Chapter 3
Emerging Applications of Microchannels

Abstract Microchannel heat exchangers have applications in several important and diverse fields including: aerospace; automotive; bioengineering; cooling of gas turbine blades, power and process industries; refrigeration and air conditioning; infrared detectors and powerful laser mirrors and superconductors; microelectronics; and thermal control of film deposition. The advantages of microchannel heat exchangers include high volumetric heat flux, compactness for space-critical applications, robust design, effective flow distribution, and modest pressure drops. This chapter will cover selected industrial examples for microchannel heat exchangers, microchannel heat pipes, and microchannel heat plates.

Keywords Automotive · Aerospace · Chemical reactor · Cryosurgery · Laser diode · Heat pipe · Pulsating · Cosmos · Heat plate

3.1 Microchannel Heat Exchangers

3.1.1 Automotive and Aerospace

Microchannel heat exchangers have at least one fluid flow passage with typical dimensions between 1 μm and 1 mm and have great potential in process intensification of various industrial areas (Fan and Luo 2008). There are many possible channel geometries for microchannel heat exchangers, two types of which are the most widely used in compact heat exchanger designs for automotive and aerospace applications. These are shown in Figs. 3.1 and 3.2. High-temperature and compact micro heat exchangers can be manufactured using ceramic tape technology (Schmitt et al. 2005), which uses fused ceramic layers to create channels with dimensions below 1 mm (Ponyavin et al. 2008). Metal-based microchannel heat

M. Ohadi et al., *Next Generation Microchannel Heat Exchangers*,
SpringerBriefs in Thermal Engineering and Applied Science,
DOI: 10.1007/978-1-4614-0779-9_3, © The Author(s) 2013

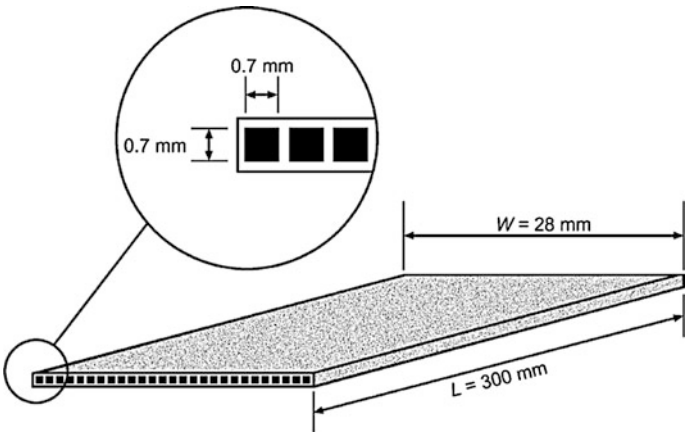

Fig. 3.1 Typical dimensions of a rectangular microchannel for compact heat exchanger applications

exchangers are also of current interest because of the combination of high heat transfer performance and improved mechanical integrity (Mei et al. 2008). Figure 3.3 shows a manufactured, flat extruded multichannel aluminum heat exchanger.

With the aim of reducing size and cost, microchannel heat exchangers are now able to achieve performances for surface area per unit volume as high as 1500 m^2/m^3. Their fin geometry is rather complex (as shown in Fig. 3.4), as they are specially designed to augment the heat transfer level on both the liquid and air sides with a balanced resistance between the two sides. Several experimental correlations for compact heat exchangers are available, but their current technical limitations may not allow for the practical design and optimization of new microchannel heat exchangers.

In recent years major progress in microchannel heat exchangers has been made by the automotive, aerospace, chemical reactor, and cryogenic industries. Thermal duty and energy efficiency requirements have increased during this period, while space constraints have become more restrictive. The trend has been toward greater heat transfer rates per unit volume. The hot side of the evaporators in these applications is generally air, gas, or a condensing vapor. With advances in the air-side fin geometry, heat transfer coefficients have increased, as have surface area densities. As the air-side heat transfer resistance has decreased, more aggressive heat transfer designs have been sought on the evaporating side, resulting in the use of microchannel flow passages on the liquid side (evaporating or condensing or single-phase regimes). The major changes in recent evaporator and condenser designs for automotive and other compact heat exchanger applications involve the use of individual, small-hydraulic-diameter flow passages arranged in a multi-channel configuration on the liquid side.

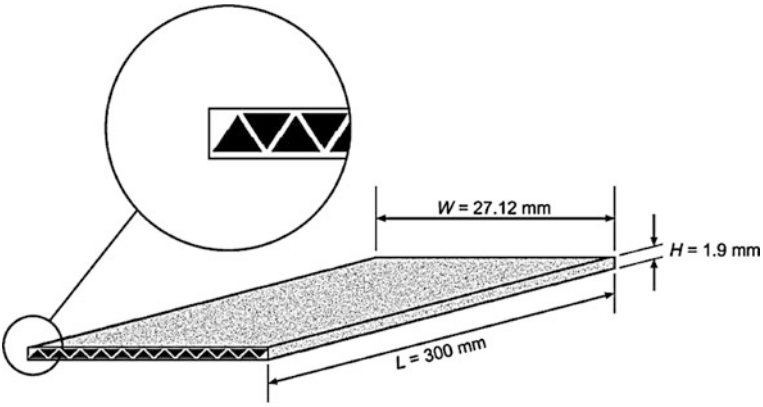

Fig. 3.2 Typical dimensions of a triangular microchannel for compact heat exchanger applications

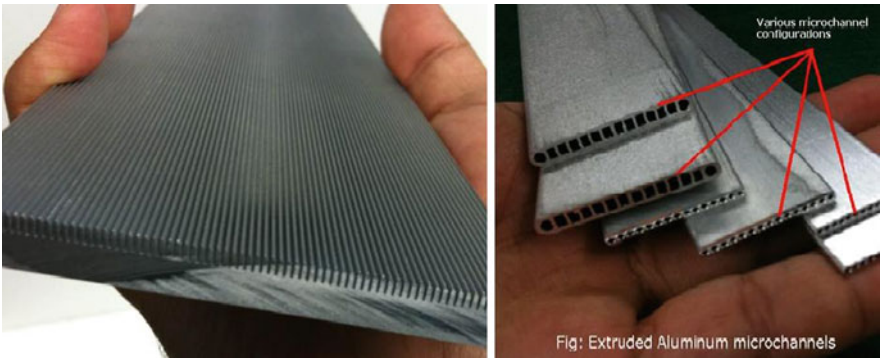

Fig. 3.3 View of a microchannel heat exchanger

The ability to efficiently transfer heat between fluids using lightweight, compact heat exchangers is important in a variety of applications, such as automobile radiators, air conditioning, and aerospace applications. Microchannel heat exchangers are well suited to these applications due to the microchannels' compactness, lightness, and high heat transfer performance.

Car radiators employ a cross flow design that allows a sufficient mass flow rate of air through the radiator while using only the stagnation pressure associated with the motion of the automobile. The common measure of performance for car radiators is the heat transfer/frontal area normalized by the difference in inlet temperatures of the coolant (water–glycol) and the air. For conventional car radiators, 0.31 W/Kcm^2 of heat transfer/frontal area can be obtained between the air and the coolant (Webb and Farrell 1990; Parrino et al. 1994). However, these radiators are extremely thick (1–2 cm) compared with the thickness of the micro heat exchanger described here (0.1–0.2 cm). Harris et al. (2000) designed and

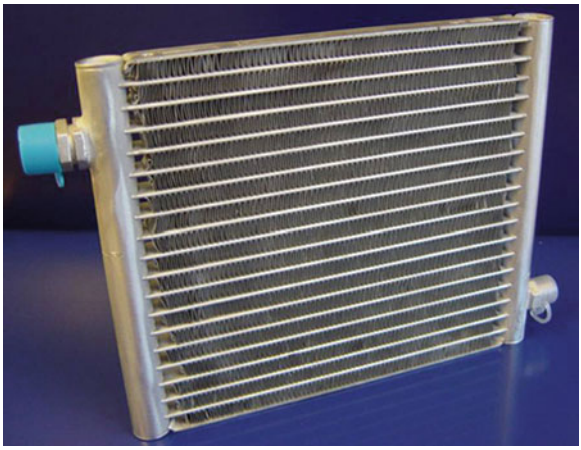

Fig. 3.4 A typical compact microchannel heat exchanger (HYBRAZ™/®)

fabricated a cross flow micro heat exchanger that transfers heat from coolant (water–glycol) to air. They used a manufacturing process that combines LIGA micromachining, traditional precision micromachining, and bonding. They compared the thermal performances of plastic, ceramic, and aluminum microchannnel heat exchangers with those of conventional car radiators. The cross flow microchannel heat exchanger can transfer more heat/volume or mass than existing conventional heat exchangers within the design constraints. This can be important in a wide range of applications (automotive, home heating, and aerospace).

Figure 3.5 shows a plate-fin evaporator geometry commonly seen in compact refrigerant evaporators for automotive and aerospace applications. As seen in the figure, fins are placed between microchannel flow slabs, and the arrangement is brazed together in a special oven. Figure 3.6 shows a manufactured aluminum microchannel heat exchanger.

3.1.2 Chemical Reactors

Microchannel chemical processing technology is an emerging field with applications in most industrial processes due to its excellent mixing capabilities, controlled reaction environment, and energy efficiency. This technology offers improvements in existing processes and will enable new processes to become cost effective. The basic microchannel reactor design is based on the flow between parallel platelets coated with a catalyst. The large aspect ratio of the channel provides extensive surface area in a small volume. Microchannel reactors have been developed based on ceramic substrates as well as metal substrates. In both types of reactors, multiple layers coated with catalytic material are bonded, forming a monolithic structure. An added benefit of a layered pattern is the ability to easily scale up or down by adjusting the number of layers. This provides great

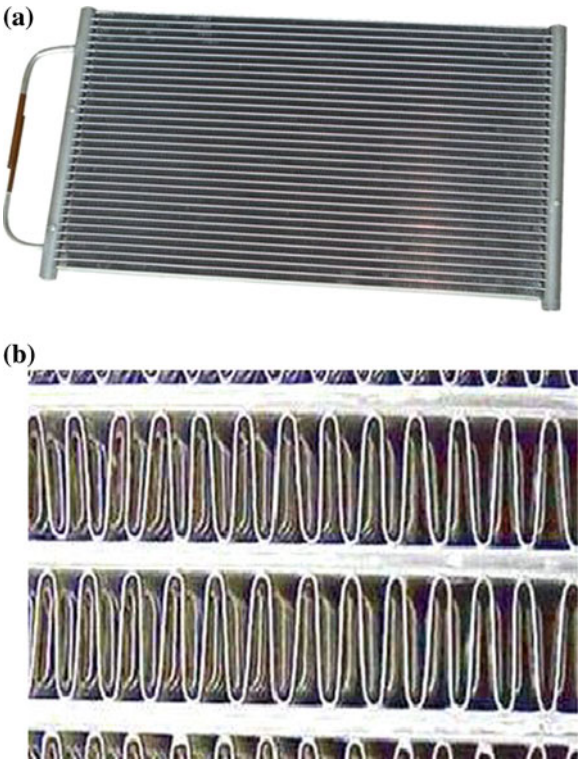

Fig. 3.5 Photographs of refrigerant and airside flow passages in a compact automotive microchannel heat exchanger. **a** A compact microchannel heat exchanger for automotive applications (Flygrow Refrigeration Co., Ltd); **b** air-side fin

Fig. 3.6 Aluminum microchannel heat exchanger (Alarko-Carrier Inc.)

flexibility in the design, since if the production capacity needs to be changed, there is no need to redesign the reactor. Figure 3.7 shows a manufactured microreactor.

Recently, microchannel heat exchangers have been widely used in fuel cell systems, which have gained increased attention in the energy system sector.

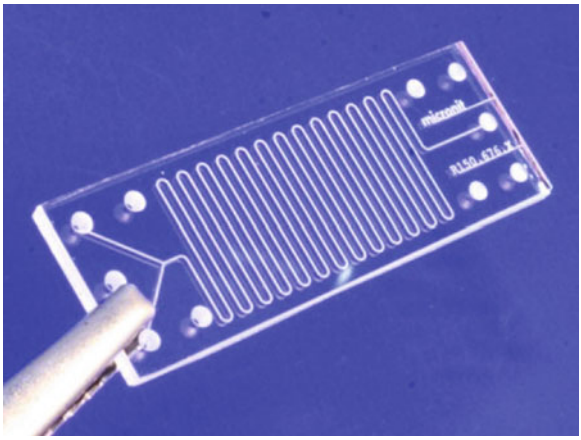

Fig. 3.7 Glass microreactor: the channels of the chip in the picture are 150 μm wide and 150 μm deep (This image was published under a Creative Commons Attribution license and appears on Wikimedia Commons at http://en.wikipedia.org/wiki/Microreactor, Micronit, Glass Microreactor made by Micronit Microfluidics, 11 August 2006, Glass-microreactor-chip-micronit.jpg)

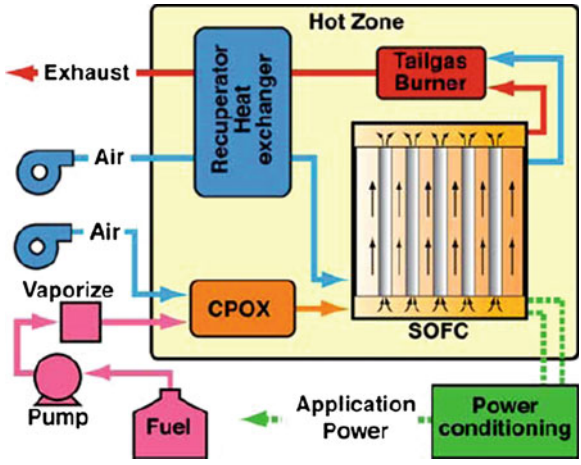

Fig. 3.8 Portable SOFC process flow diagram (Murphy et al. 2011)

The thermal integration of heat exchangers and chemical reactors is essential for effective operation of solid oxide fuel cell (SOFC) systems. In Fig. 3.8, a partial-oxidation reactor, a catalytic tail-gas combustor, and a cathode-air preheating recuperator are shown as separate unit processes. However, system efficiency can be improved and costs reduced via process intensification, which combines unit processes. Figure 3.9a is an exploded view illustrating the internal geometry for two layers of microchannels, with a photograph of the microchannel reactor shown in Fig. 3.9b. The current reactors use four layers, two reacting and two non-reacting, and can be configured as required for different applications (such as steam reforming or catalytic partial oxidation). Microchannels within the reacting layers are washcoated with an Rh-catalyst for fuel reforming. The hot gases flowing through the non-reacting layers heat the fuel and drive the upstream fuel-reforming processes within the reactive channels. The current reactors are

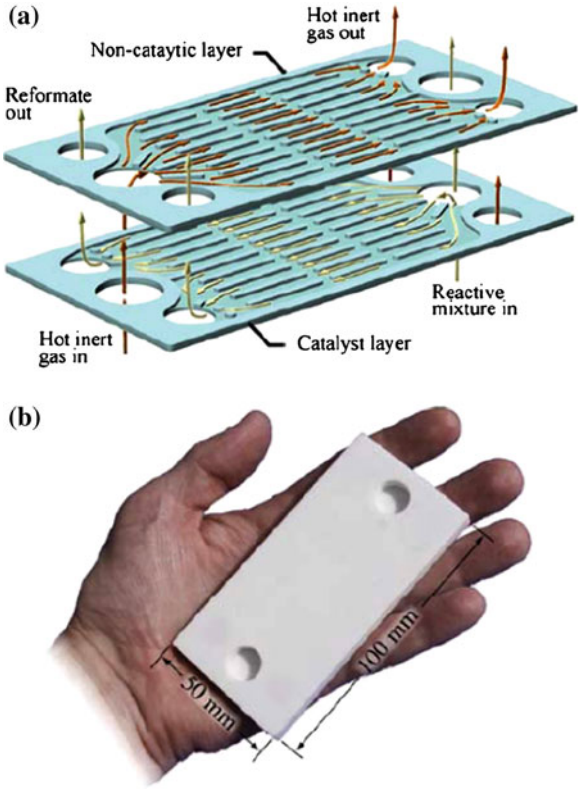

Fig. 3.9 **a** Exploded illustration of two layers of the ceramic microchannel reactor, and **b** photograph (Murphy et al. 2011)

fabricated by CoorsTek, Inc. (Golden, Colorado, USA) using 94 % alumina. A new fabrication process (called Pressure Laminated Integrated Structures, or PLIS) enables cost-effective manufacturing.

The performance advantages of microchannel reactors, including integrated chemical processing, are well documented (Kandlikar et al. 2006; Yarin et al. 2009; Anxionnaz et al. 2008). The fine channels utilized in such reactors enable exceptional control of thermal processes, enabling tight regulation of chemical reactions for achieving desired operating conditions. This thermal control results in higher product yields and selectivity, optimal catalyst activity, longer catalyst lifetime, and higher overall reactor productivity.

A recent review by Sommers et al. (2010) discusses numerous applications that particularly benefit from ceramic heat exchangers. Ceramic materials offer potentially significant advantages compared to metal alternatives, including significantly higher operating temperatures, improved tolerance of harsh chemical environments, improved bonding with ceramic-based catalyst washcoats, and significant cost savings in materials and manufacturing methods. Although there are numerous possible applications, the effort reported here is motivated by the need for low-cost, high-performance fuel reformers, and the need to effectively

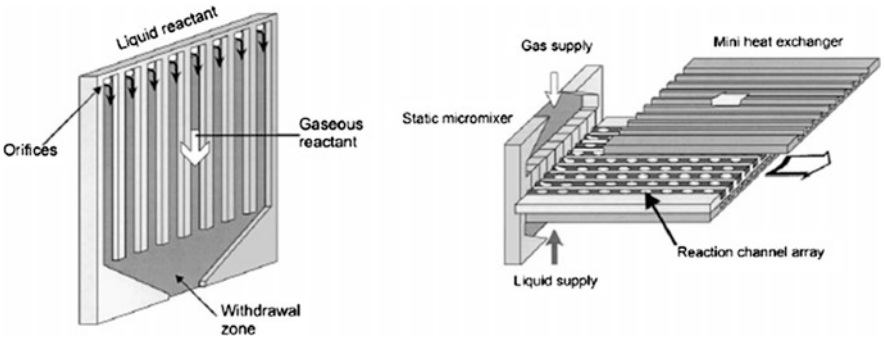

Fig. 3.10 Falling film and microbubble reactors (Jahnisch et al. 2000)

integrate unit processes in solid-oxide fuel cell systems. The microchannel reactor integrates the upstream fuel heating and reforming with downstream recuperation to harness the high-quality heat exiting the tail-gas combustor. Such process intensification can improve system efficiency. It is feasible to further combine processes by catalytically activating both sides of the microchannel reactor, using one set of layers for upstream fuel reforming and the opposite set for tail-gas combustion.

Falling-film microreactors work in the same way as macro-scale absorbers. Microchannel falling-film absorbers have been reported in the open literature by Goel and Goswami (2007), Hessel et al. (2005), Jahnisch et al. (2000), and Zhang et al. (2009). The central part of the microreactor is a stainless steel plate containing 64 vertically positioned microchannels (300 μm wide and 100 μm deep). Liquid spreads to form a thin film among the microchannels and flows further downward to the withdrawal zone at the bottom. Gas flows in a large gas chamber positioned above the microchannel section, facilitating concurrent or countercurrent operation mode. Figure 3.10 shows a schematic of a falling-film and microbubble reactor.

In membrane separation technology, gas and liquid flow in two different channels, separated by some physical structure, such as a mesh, selective membrane, or micro-porous plate (Abdallah et al. 2004). Oak Ridge National Laboratory and Velocys Inc. separated liquid and vapor phases in microchannels by membrane in a traditional counter-flow arrangement. The membrane prevents the liquid from bridging the microchannel and maintains stable phase separation. However, it significantly decreases the surface area of the liquid–gas interface. Figure 3.11 shows the opening area of the membrane comprising just about 10 % of total surface area.

In the co-current configuration, gas, and liquid flow concurrently in the same microchannel, creating various types of flow patterns similar to that of two-phase flow in a tube. The liquid film is maintained by shear stress of the moving gas phase, and film thickness can be ultimately small. Channel hydraulic diameter can be significantly smaller, limited only by the desired fouling characteristics.

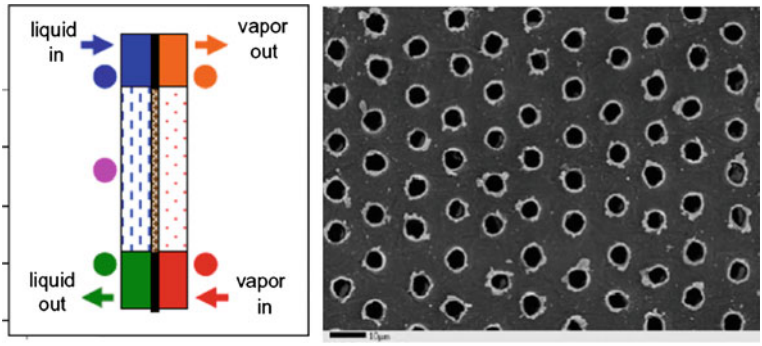

Fig. 3.11 Counter-flow absorber and phase separating membrane (Velosys Inc.)

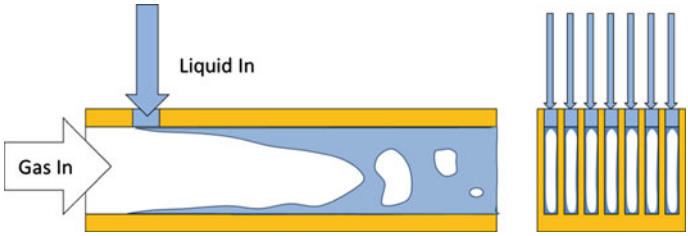

Fig. 3.12 Co-current microchannel absorption process (Jenks and Narayanan 2008)

With co-current flow, films of a few microns thick can be arranged on the channel wall, and associated with this thickness very high mass transfer coefficients can be obtained (Jenks and Narayanan 2008). Figure 3.12 shows a schematic of the co-current microchannel absorption process.

Yue et al. (2008) experimentally investigated hydrodynamics and mass transfer characteristics in co-current gas–liquid flow (CO_2/water) through a horizontal rectangular microchannel with a hydraulic diameter of 667 μm. Liquid-side volumetric mass transfer coefficient and interfacial area in the present microchannel were measured as high as 21 s^{-1} and 9000 m^2/m^3, respectively, which are at least one or two orders of magnitude higher than those in conventional gas–liquid contactors. This shows the great potential of gas–liquid micro-chemical systems for many industrially relevant gas–liquid mass transfer operations and reactions.

3.1.3 Cryogenic Systems

Microchannel heat exchangers are used in cryosurgical probes for ablating tumors or treating heart arrhythmia (Marquardt et al. 1998), as shown in Fig. 3.13. The Joule–Thomson cryocooler is most widely used for the cryosurgical probe.

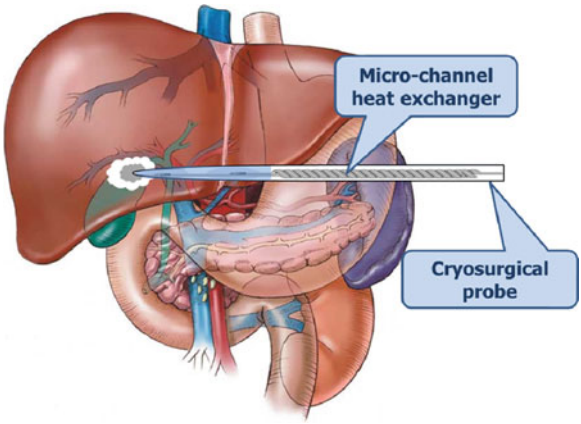

Fig. 3.13 Treatment of a cancer by cryosurgery

The advantages of the Joule–Thomson cryocooler include its simple structure and compactness and the lack of electrical interference. The heat exchanger of the subminiature Joule–Thomson refrigerator used in the cryosurgical probe has channel diameters from tens of microns to hundreds of microns, according to space limitations. Figures 3.14 and 3.15 show schematic diagrams of a cryosurgical probe and a Joule–Thomson cryocooler, respectively. As shown in Fig. 3.15, the Joule–Thomson cryocooler includes a counter-flow heat exchanger, a Joule–Thomson valve to decrease refrigerant temperature through an isenthalpic expansion process, and an evaporator to absorb external heat. Figure 3.16 shows a cryosurgical system for use in cancer surgery.

Until recently, the subminiature Joule–Thomson refrigerators in most commercialized cryosurgical probes have used a high pressure argon gas as the refrigerant in an open system. However, a closed system with a mixed refrigerant is desirable, since the efficiency of the Joule–Thomson refrigerator with a pure refrigerant is much lower than that possible with a mixed refrigerant. A closed-system cryosurgical probe with a mixed refrigerant is feasible because a mixed refrigerant decreases the working pressure of the refrigerator. The most important parameter to optimize in a Joule–Thomson refrigerator using a mixed refrigerant is the combination of the mixed refrigerant for high and low pressure conditions. In particular, pressure drop within the microchannel heat exchanger must be optimized to obtain optimal performance from the refrigerator.

Plants that liquefy natural gas are another application field of microchannel heat exchangers. Natural gas is liquefied at temperatures around −161 °C (112 K) (Waldmann 2008). The composition of natural gas depends on the well from which it is extracted, but most natural gas consists of methane (CH_4). Both global and domestic demand for liquefied natural gas (LNG), with its advantages for transportation and energy density, are currently increasing. LNG was the source of 25 % of world energy consumption in 2005, but this demand will increase up to 50 % in the next 10 years. Because 20 % of natural gas wells are under the sea, offshore gas plant development is being re-evaluated as a promising energy

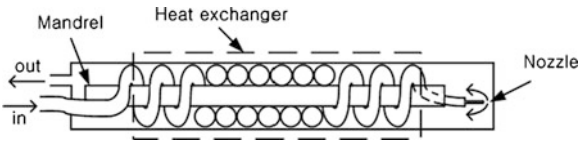

Fig. 3.14 Schematic diagram of a cryosurgical probe

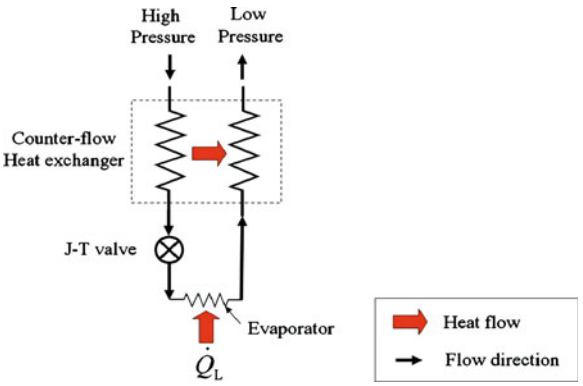

Fig. 3.15 Schematic diagram of a Joule–Thomson cryocooler

Fig. 3.16 Cryosurgical system for surgery of cancer (This image was published under a Creative Commons Attribution license and appears on Wikimedia Commons at http://en.wikipedia.org/wiki/File:Cryogun.jpg, Warfieldian, Medical cryotherapy gun used to treat skin lesions, 18 July 2011)

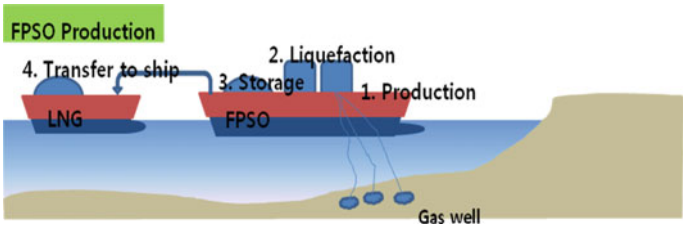

Fig. 3.17 Floating production storage and offloading method (Baek et al. 2010)

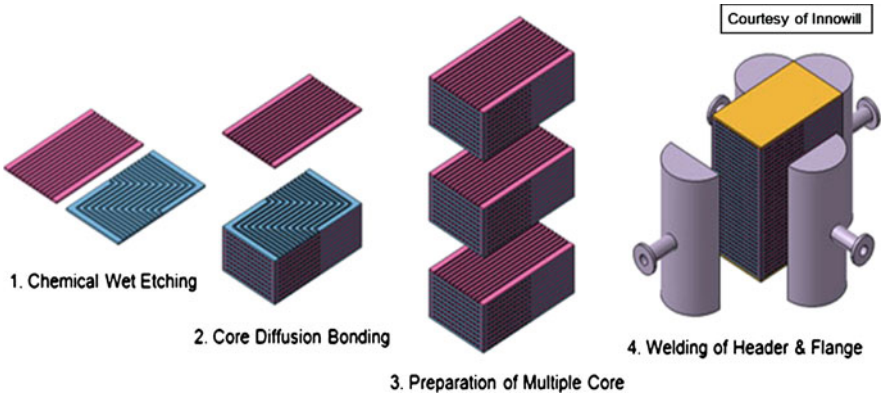

Fig. 3.18 Microchannel heat exchanger for FPSO (Baek et al. 2010)

industry. Floating production storage and offloading (FPSO) plants refine, liquefy and store natural gas from the sea. This LNG production method has a big advantage in that there is no need to transfer the natural gas from an offshore drilling rig to an onshore plant to liquefy it. An FPSO plant can also transport LNG to another ship, which is cost effective. The FPSO method is shown in Fig. 3.17.

There are some technical constraints (lightness of the ship, compactness, safety) for FPSO plants because many types of equipment must be loaded on the comparatively small ship. However, compactness and lightness can be achieved by using the proper equipment. One of the largest pieces of equipment in an LNG plant is the heat exchanger, and thus, if the size of the heat exchanger can be reduced, the size of the entire facility can be reduced. Microchannel heat exchangers can be used to achieve this goal. A compact heat exchanger for FPSO constructed by the etching method and diffusion bonding is shown in Fig. 3.18. A manufactured microchannel heat exchanger for FPSO is shown in Fig. 3.19. Microchannel heat exchangers for FPSO have the advantage of compactness, but they also have a disadvantage in performance due to axial conduction, especially in cryogenic applications (Maranzana et al. 2004). In many cryogenic applications, the desired heat transfer, which is the refrigeration load, is a small fraction of the heat transferred within the heat exchanger. In this case, the ineffectiveness of the

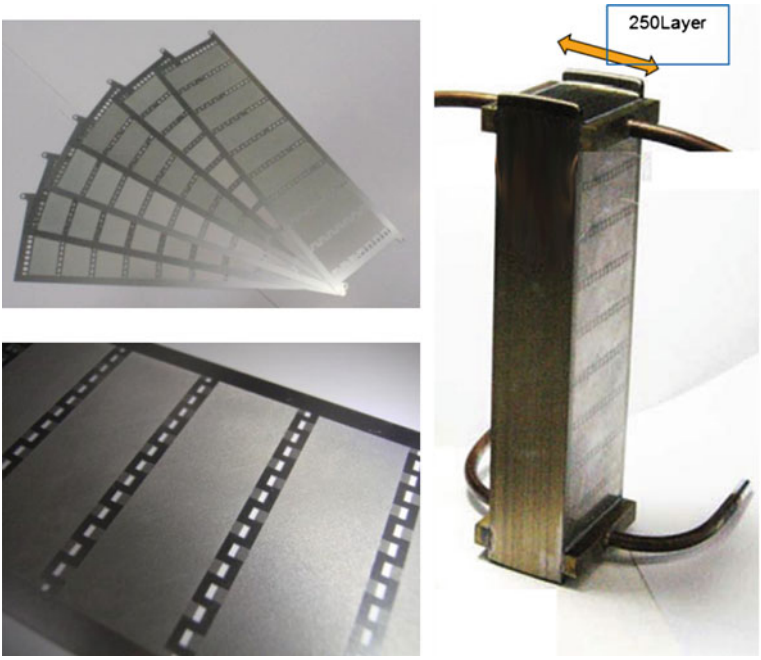

Fig. 3.19 Microchannel heat exchanger for an FPSO (Kim et al. 2010)

heat exchanger must be an even smaller number, and the effect of axial heat conduction and parasitic heat transfer can dominate the performance of the device (Nellis 2003). Furthermore, the large absolute temperature change within the heat exchanger produces correspondingly large variations in the properties of the fluids and metal that can also affect performance.

3.1.4 Laser Diode Applications

Microchannel cooling is now a mature technology, over 30 years old and widely used on a commercial basis in the high-power laser diode industry. Microchannel coolers are also now being used in commercial systems to cool LEDs in UV curing systems and photovoltaic cells in concentrated solar power systems. The present commercial cooling technologies, however, will not be adequate as power levels of semiconductor devices increase. Since laser diodes have stringent performance requirements and are by far the largest commercial market share of microchannel coolers, the remainder of this discussion will focus on laser diode applications.

Commercial coolers generally employ water-cooled copper microchannels to dissipate up to 1 kW/cm^2 from semiconductor heat sources ranging from 0.1–2 cm^2 in size. These coolers use rectangular ducts with widths from

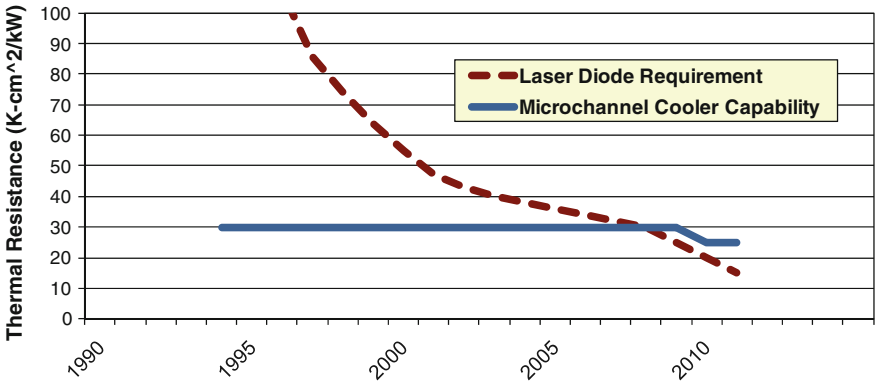

Fig. 3.20 Microchannel cooler capability versus laser diode requirements

25–200 μm, duct aspect ratios up to 15X, and flow rates ranging from 10–30 gm/cm^2/W (based on heated area). These parameters result in thermal resistances of 30–75 K-cm^2/kW, with pressure losses between 10 and 50 psi.

Laser diodes stress thermal management capabilities due to their low allowable junction temperatures (<70 °C) and large waste heat fluxes. Historically the capabilities of microchannel coolers have exceeded the most demanding laser diode requirements, accommodating heat fluxes up to 1 kW/cm^2 (Fig. 3.20). However, the operating power of laser diodes has continuously increased, and currently prototype systems with heat fluxes up to 2.5 kW/cm^2 are being considered, suggesting that for allowable temperature differentials of 30–50 °C, future microchannel coolers must be able to operate at thermal resistances from 12 to 20 K-cm^2/kW. Unless heat spreaders are employed, this is beyond existing commercial capability.

There are four main ways future commercial microchannel systems can be improved: (1) reducing the cooler thermal resistance; (2) reducing package thermal resistance through use of reduced thermal expansion coolers; (3) reducing flow rate to minimize system costs of cooling; and (4) increasing operating lifetime.

Reducing thermal resistance is critical to the continued increase in laser diode array brightness. Methods under consideration for this task include reducing channel widths, adding secondary features, such as fins or perforations, and using high conductivity materials such as CVD diamond. Reducing channel width is promising: for water-cooled systems, reducing the channel width of a copper microchannel cooler to ~12.5 μm results in thermal resistances in the 15–20 K-cm^2/kW range with reasonable pressure losses. Secondary features can offer performance improvements for larger channels (channel width >100 μm), but they cannot be economically fabricated in smaller channels.

Diamond is well known for its outstanding thermal conductivity, but it is difficult to machine with micropassages. Figure 3.21 shows a prototype diamond microchannel cooler fabricated by laser etching thin (100 μm thick) diamond

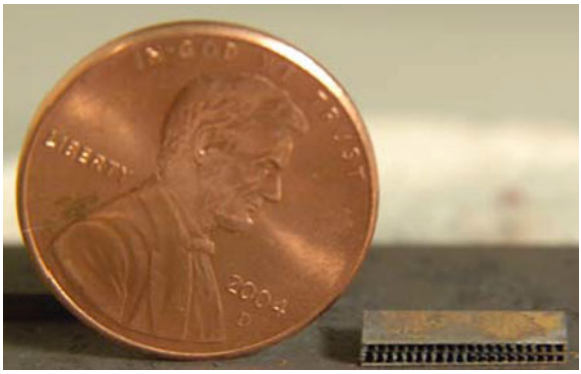

Fig. 3.21 CVD diamond microchannel cooler with 250 × 300 μm rectangular ducts (Campbell et al. 2006)

sheets and brazing the sheets together. This approach was not able to create passages narrower than 250 μm.

Many laser diode packages employ fairly thick ceramic carriers (on the order of 250 μm) to accommodate the thermal expansion mismatch between the GaAs diode (CTE = 6.9 μm/m/K) and the copper cooler (CTE = 16.6 μm/m/K). These carriers have thermal resistances comparable to that of the cooler itself. Coolers fabricated using low expansion materials can reduce the thermal expansion significantly, with only small penalties in thermal resistance.

Figure 3.22 shows two versions of reduced expansion coolers. Microchannel coolers offer promise for cooling systems with large numbers of semiconductors, such as MW-class laser systems and radar arrays. The system-level coolant requirements are very large and represent a significant barrier to deployment of these systems. Refrigeration or two-phase cooling loops can reduce coolant usage, so long as the thermal resistance is not compromised. While promising two-phase microchannel research has been conducted over the past decade, two-phase systems remain immature. More work is required to implement research results in the marketplace.

As microchannel coolers have evolved from an exotic technology to a commonplace component, their required operating lifetime has increased from 3×10^3 to 10^4 h. In radar cooling applications the lifetime may be expected to be as high as 10^5 h. At the high flow rates required to achieve the lowest thermal resistances, erosion can limit the performance of a cooler to $\sim 10^3$ h. Corrosion is also a critical concern. Internal protective coatings are now being investigated to reduce susceptibility to erosion and corrosion.

3.1.5 Enhanced Micro-Grooved Tubular Evaporators for Waste Heat Recovery Applications

As much as 50 % of industrial energy is lost as waste heat in the form of energy in exhaust gas streams, cooling water and heat losses from hot equipment surfaces and heated products. To improve energy efficiency—and thereby reduce the

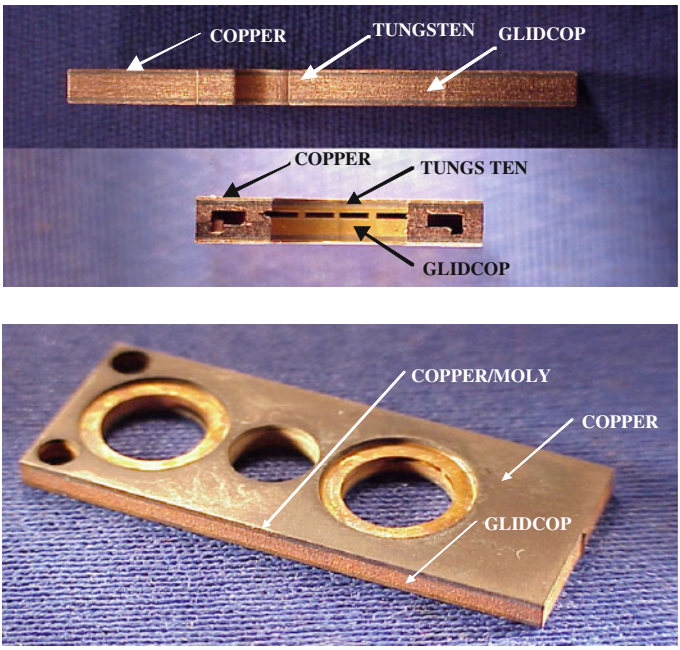

Fig. 3.22 Examples of reduced thermal expansion format microchannel coolers (Campbell et al. 2006)

emissions and cost associated with the energy resources—cost effective utilization of waste heat is of strong interest to many industrial sectors. Numerous technologies are commercially available for large-scale systems to tap waste heat and improve energy productivity. In some cases, waste heat recovery technologies have increased energy efficiency as much as 50 %. However, heat recovery is not economical for small-scale applications due to high capital costs. High system cost and heavy weight/volume of the associated equipment prevent the use of these technologies in smaller scale waste heat-to-cooling applications. This section describes the development of a high-performance, compact evaporator and condenser that will potentially reduce weight, volume, and cost of heat energy recovery as well as other energy conversion systems. The method uses an innovative microchannel technology combined with a force-fed fluid manifold system to enhance the heat and mass transfer in the evaporators and condensers.

Details of the novel force-fed microchannel technology used in this case are discussed in the literature (Baummer et al. 2008). Heat flux levels above 1100 W/cm^2 with h values above 200,000 W/m^2 K are reported using HFE7100 as the working fluid for electronics cooling applications. Compared to traditional microchannel design, very high heat transfer coefficients were obtained due to secondary flows and creation of evaporating thin liquid films. Also, the manifold system for guiding the flow reduced the length of the flow passes significantly and hence minimized the pressure drop. More recently, micro-structured surface

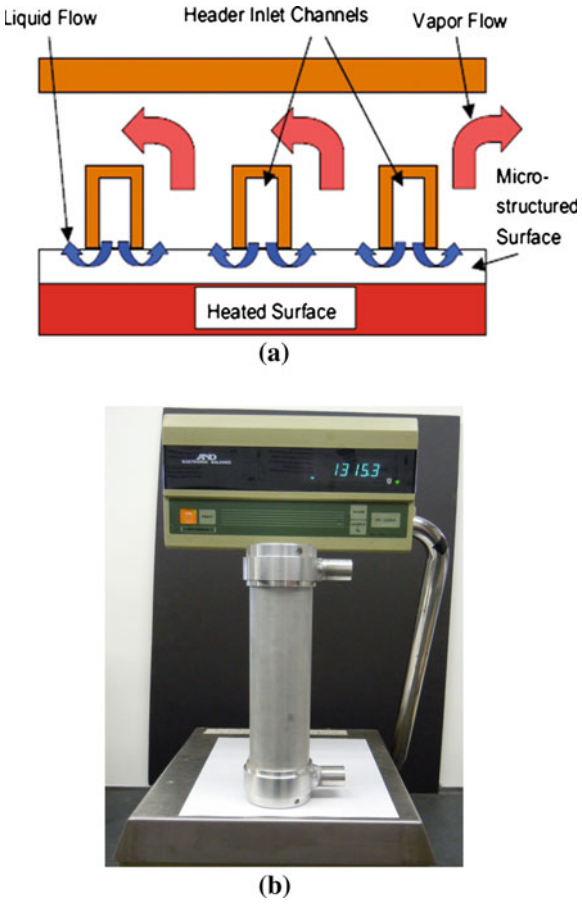

Fig. 3.23 **a** Schematic of the force-fed evaporation process; **b** tubular evaporator (Jha et al. 2011)

evaporators and condensers were repackaged to a tubular configuration to simplify fabrication and increase operation pressure. The first published information about tubular configuration is presented in (Jha et al. 2011).

A diagram of the force-fed evaporation process is shown in Fig. 3.23a. The process uses an inlet header positioned on top of the micro-structured surface to direct the working fluid into the surface. The working fluid evaporates as it passes through a heated surface, and vapor flows out of the channels back into the header and finally exits the header through alternate manifold channels. Figure 3.23b shows the fabricated tubular evaporator. The approximate weight of the evaporator is 1.3 kg, and it is roughly 60 mm in diameter and 250 mm in length.

A schematic of the experimental setup for investigating the heat transfer and pressure drop characteristics is shown in Fig. 3.24. The evaporator design was tubular and utilized microgrooves on the outer side and minigrooves on the inner side of the tubular surface for enhancing the heat transfer coefficient on both sides, thus improving the cooling capacity. The outer side is used for refrigerant (R134a)

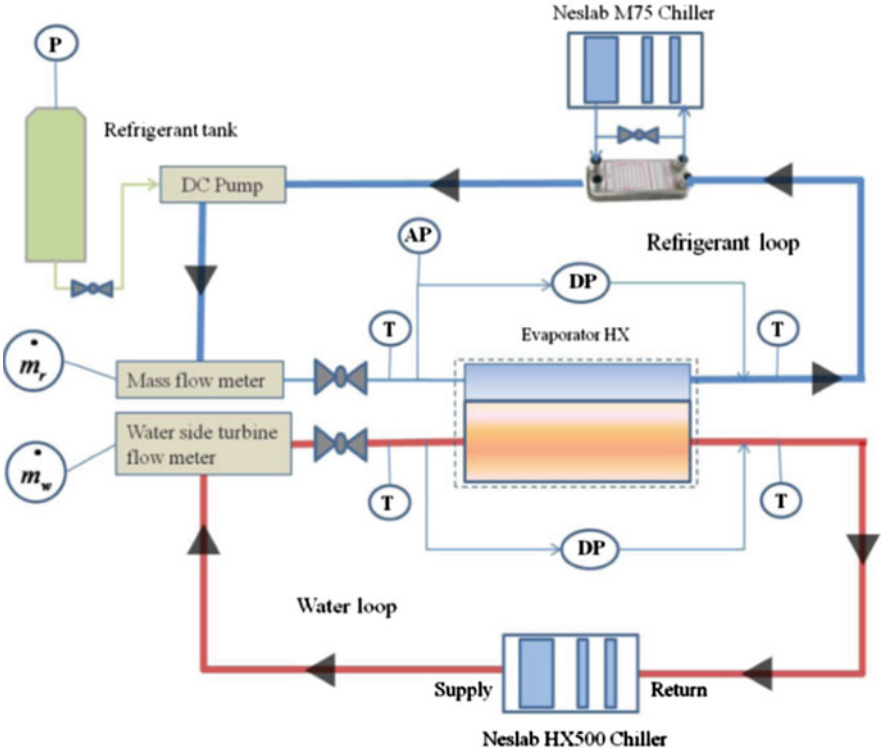

Fig. 3.24 Schematic of the experimental setup (Baummer et al. 2008)

flow, where medium aspect ratio microgrooves with hydraulic diameter of 150 μm and inner side minigrooves with hydraulic diameter of 600 μm were used. The HX tube was fabricated at Wolverine MicroCool Inc., utilizing patented micro-deformation technology to attain medium to high aspect ratio channels. The heat transfer surface was made of aluminum.

The water was supplied to the system through a Neslab Chiller HX500 with an operating temperature range of 5–35 °C. To protect the heat exchanger from corrosion, 1 g potassium silicate solution per liter of water was added. The water flow rate is measured through a water-side turbine flow meter, which is accurate to 1.5 %. An ABB K-5 flow meter was used for measuring the refrigerant-side flow rate, and a 24 V DC pump was used for varying the refrigerant flow rate in the system. A parallel plate condenser condenses the outlet refrigerant, which was cooled by a Neslab M75 chiller. On the refrigerant side, the system was completely evacuated before charging the refrigerant into the system. To ensure there is no leakage, system pressure was monitored through the data acquisition system for an entire day.

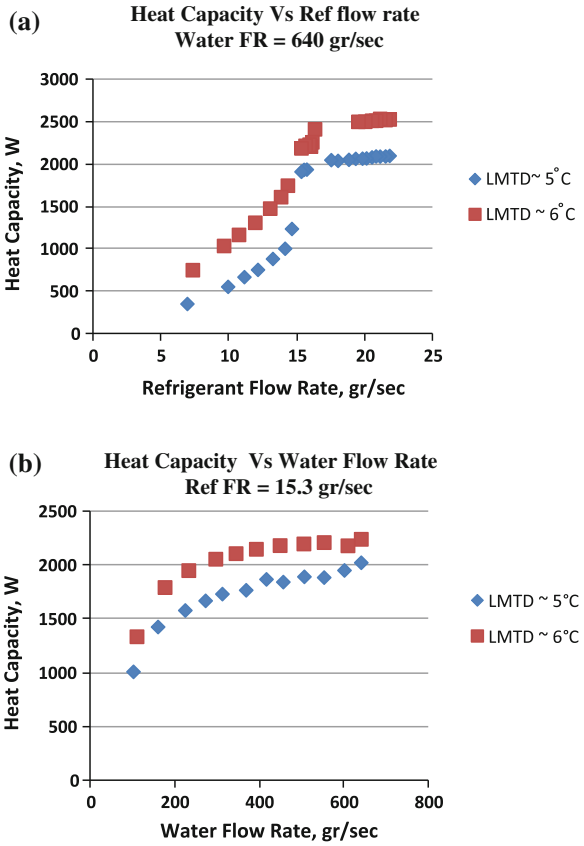

Fig. 3.25 Cooling capacity variation **a** with refrigerant flow rate for constant water mass flux; **b** with water flow rate for constant refrigerant mass flux

The evaporator test section had four T-type thermocouples at each measuring point—the inlet and exit for both the water and refrigerant sides. All thermocouples were calibrated within 0.05 °C. Differential pressure was also measured on both sides to measure the associated pressure drops. Absolute pressure measurement was required on the refrigerant side to determine the thermodynamic state of the refrigerant. All the measurements were recorded through the data acquisition system into a PC for constant monitoring and data logging.

Experimental data were collected for both constant water mass flow rate and constant refrigerant mass flow rate, as shown in Figs. 3.25a, b, respectively. Data are presented for two different sets of LMTDs (5 and 6 °C on average). Cooling capacity was observed to increase with increase in refrigerant flow rate in the lower mass flux range due to superheating of the vapor.

With variation in water mass flow rate, heat transfer rate was observed to increase for lower mass flux but to asymptote for medium and higher mass flux with a maximum uncertainty of ±15 %. Heat transfer in excess of 2 KW was observed at water mass flow rate from 200 to 640 ml/s for different LMTD values. Refrigerant mass flux was kept constant at 15.3 g/s.

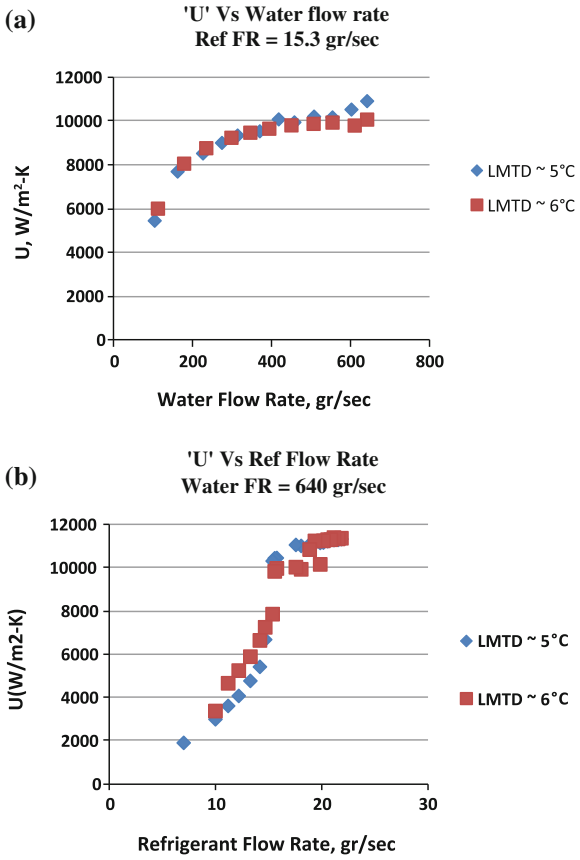

Fig. 3.26 Overall heat transfer coefficient variation **a** with water mass flow rate; **b** with refrigerant flow rate

As shown in Fig. 3.26a, the overall heat transfer (U) coefficient increases with increase in water mass flow rate until it levels off at a mass flow rate of about 400 gm/s where it attains 10,000 W/m^2 K. With further increase in mass flow rate of water only modest improvement in the heat transfer coefficient was observed.

Variation of the overall heat transfer coefficient (U) with increasing refrigerant mass flow rate is shown in Fig. 3.26b. As seen there, U does seem to asymptote as water-side heat transfer coefficient levels off. Due to fabrication limitations, the inner-side channels (water side) were mini channels with hydraulic diameter of 600 μm. Pressure drop was found to increase with mass flow rate for both refrigerant and water sides. Pressure drop was in excess of 150 mbar on the water side at 640 ml/s and 60 mbar on the refrigerant side at 22 g/s, as shown in Fig. 3.27a and b, respectively. Water side pressure drop curve varies exponentially with increasing water side flow rate.

The heat exchanger was further modified and a high aspect ratio microgrooved tube was used with 110 μm hydraulic diameter for the grooves and with an enhancement insert on the water side. The modifications increased performance of

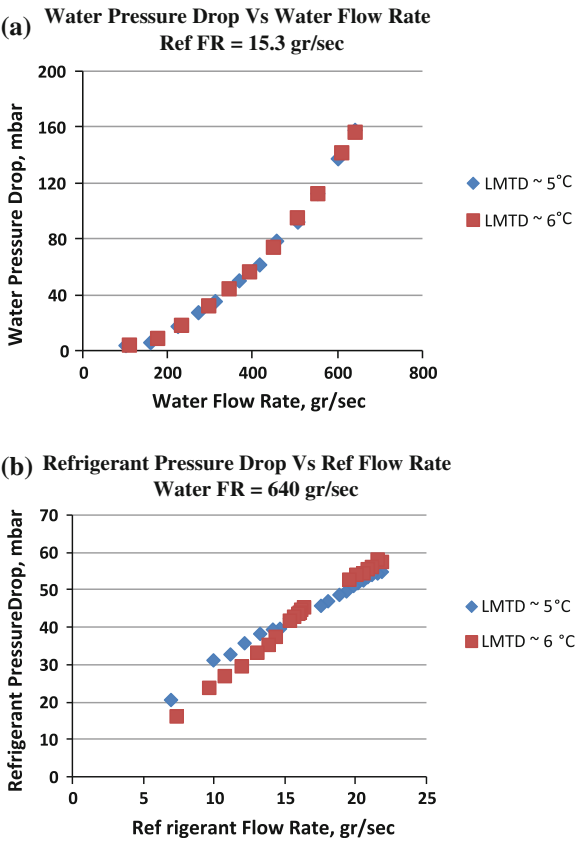

Fig. 3.27 Water side (**a**) and refrigerant side (**b**) pressure drop

the heat exchanger while reducing its pressure drops. As shown in Figs. 3.28a, b, the heat transfer rate and the capacity of heat exchanger substantially increased, with the overall heat transfer coefficient reaching a level of 20,000 W/m^2 K (Fig. 3.29). Pressure drops on both sides of the heat exchanger were almost equal and on the order of 100 mbar (Fig. 3.30a, b) or less.

3.1.5.1 Manifolded Micro-Groove Condenser

Two-phase loops have many advantages over single-phase cooling loops in electronics cooling. Two-phase loops are more compact, require much less pumping power, are lighter and require much less working fluid. Two-phase loops also provide much greater heat transfer coefficients of evaporation and condensation resulting in the reduction of size and weight of heat exchangers, which is especially important in some applications, such as space/aerospace applications. The condenser described below utilizes the manifolded, micro-groove surface technology, which was described in Chap. 2 in detail. This design involves

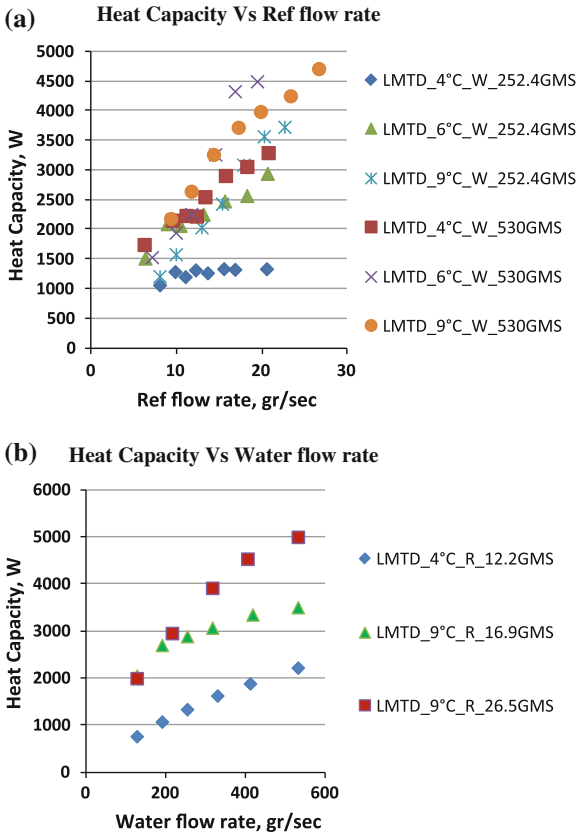

Fig. 3.28 Variation of heat transfer capacity of tubular heat exchanger with variation of refrigerant (**a**) and (**b**) water flow

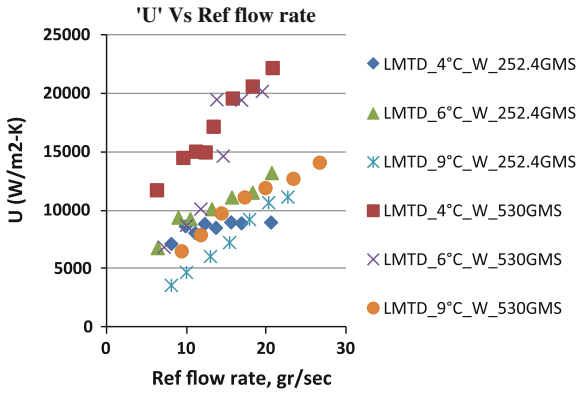

Fig. 3.29 Overall heat transfer coefficient of microgrooved surface tubular heat exchanger

manifolds that force-feed the cooling fluid through narrow channels within the micro-structured surface for only a short distance. This novel concept combines the high heat transfer rates that are generated within narrow microchannels but

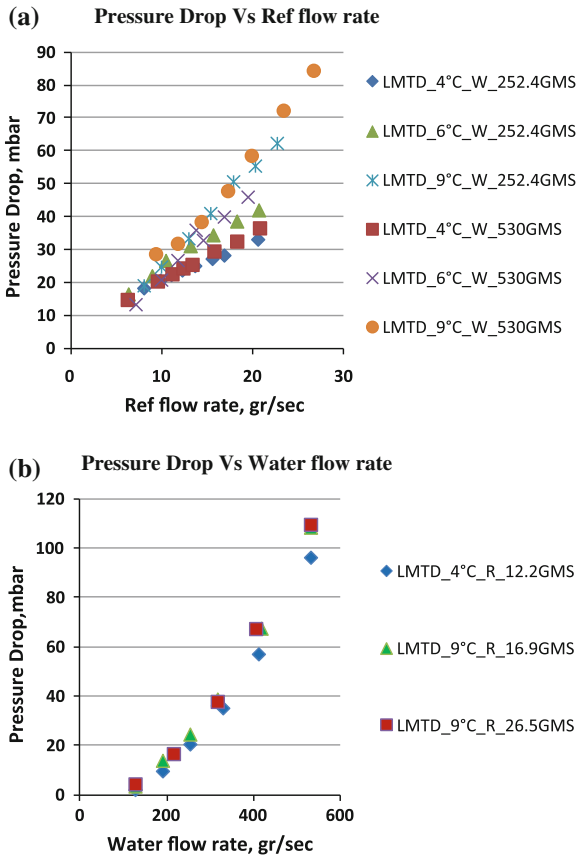

Fig. 3.30 Pressure drop of refrigerant side (**a**) and water side (**b**) of microgrooved surface tubular evaporator

without the high pressure drops of conventional microchannel geometries. As described below this geometry also works well as a condenser for two-phase flow applications.

Condenser Design

A schematic diagram of a tubular micro-groove condenser is shown in Fig. 3.31. This condenser is a tubular variant of micro-grooved surface heat exchanger. A tubular configuration is compact, allows high pressure operation, and can be assembled without permanently bonding the heat exchanger components. The condensation process in the micro-grooves is identical in the cylindrical and rectangular geometries, since the curvature in the cylindrical tube is large compared with the depth of the micro-grooves. The tubular heat exchanger consists of a micro-grooved tube and internal and external flow distributors, which are placed in the cylindrical body of the heat exchanger and sealed with flanges.

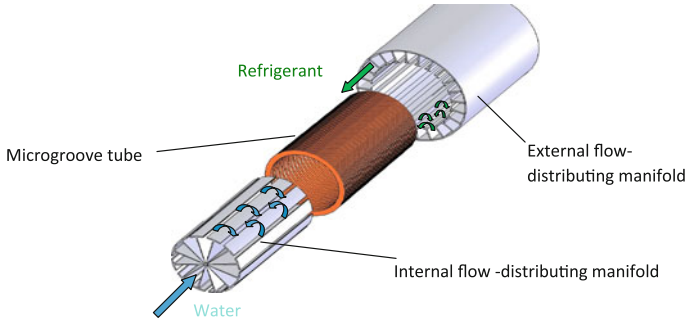

Fig. 3.31 Schematic diagram of a tubular condenser

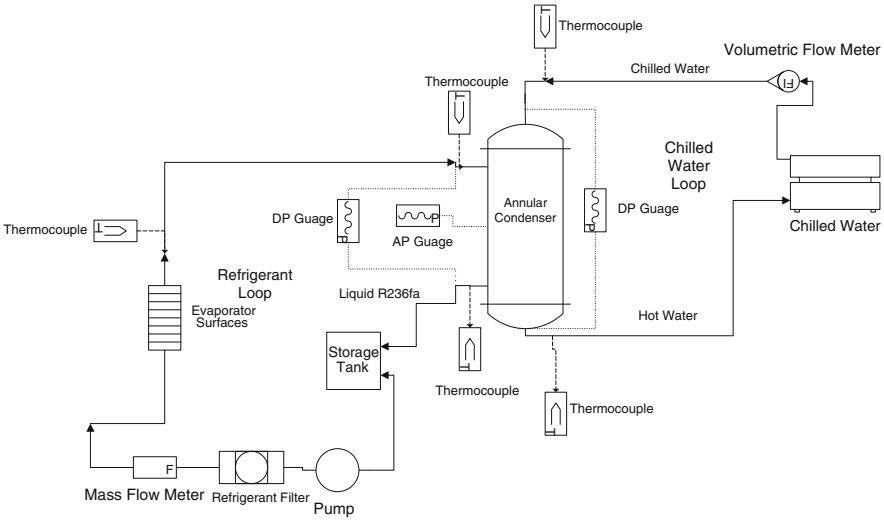

Fig. 3.32 Schematic diagram of R134a condenser test setup

Heat Transfer Testing Loop

The test loop, shown in Fig. 3.32, included the following components: evaporator, condenser, water chiller, storage tank, pump, mass flow meters (water and refrigerant), thermocouples, differential pressure sensor, and absolute pressure sensor. A photograph of the testing loop is shown in Fig. 3.33. The evaporator for the testing loop consisted of a thin-wall stainless steel tube heated directly by electrical current passing through it. The low electrical resistance of the metal requires electrical current in excess of 250 A; therefore, a high current transformer was used as a power source (see Fig. 3.34). The heater is in the bottom center part of the photograph with a storage tank attached to its housing.

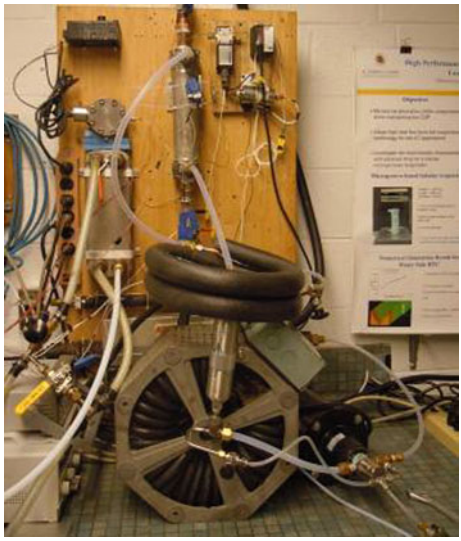

Fig. 3.33 Photograph of the new equipment to achieve higher flow rates and pressures

Fig. 3.34 Photograph of the electrical heater and heating coil

Determination of Refrigerant and Water-Side Heat Transfer Coefficients

In order to determine the heat transfer coefficient of the refrigerant side (h_{ref}), one first needs to measure the overall thermal resistance, U,

$$\frac{1}{U * A} = \frac{1}{h_{ref} * A} + \frac{1}{h_{wtr} * A} \tag{3.1}$$

The total or overall heat transfer coefficient (U) is made up of the water side heat transfer coefficient (h_{wtr}), and refrigerant-side heat transfer coefficient h_{ref}. In order to calculate h_{ref} we must first calculate the other two. U is calculated using the following formula. (Fernandez-Seara et al. 2007):

$$U = Q_{\text{wtr}}/(A * \text{LMTD}) \tag{3.2}$$

where Q_{wtr} is the cooling load and is calculated by using the water-side data for a single-phase heat transfer process.

$$\dot{Q}_{\text{wtr}} = \dot{m}_{\text{water}} * c_{p_{\text{water}}} * (T_{\text{waterout}} - T_{\text{waterin}}) \tag{3.3}$$

LMTD is the log mean temperature difference and is calculated as:

$$\text{LMTD} = \frac{T_{\text{wout}} - T_{\text{win}}}{\ln \frac{T_{\text{win}} - T_{\text{sat}}}{T_{\text{wout}} - T_{\text{sat}}}} \tag{3.4}$$

Here, h_{wtr} is only a function of $\dot{m}_{\text{water}}$, and since it is single phase and the temperature change is small, we can assume constant fluid properties. Thus, h_{wtr} can be assumed to be a function of Reynolds number or water velocity. A study was done to find the correlation between the h_{ref} and V_{wtr}. In order to do this h_{ref} needed to be kept constant. $h_{\text{ref}} = f(q'', T_{\text{sat}}, \dot{m}_{\text{ref}})$, so as long as the refrigerant mass flow rate, system pressure and Q_{out} were kept constant then h_{ref} would not vary. It was assumed that h_{wtr} is proportional to V^n, and Eq. (3.1) becomes (Fernandez-Seara et al. 2007):

$$\frac{1}{U} = K + C * \frac{1}{V^n} \tag{3.5}$$

The constant C has obtained the slope of the $1/U$ curve plotted against $1/V^n$. A range of U and V values were obtained from running a test matrix that varied water flow rate between 3 and 7 GPM and inlet water temperature between 14 and 18 °C.

The resulting data sets were grouped together at constant T_{sat}, m_{ref}, and Q_{out} values, and each data set was graphed. The next step would be to determine the optimal value of 'n' in Eq. (3.5). If the value of n is correct then the standard deviation between the values of 'C' for each test would be ~ 0. By varying the values of n between 1.1 and 0.5 and plotting the standard deviation versus n we can see that there is an optimal point where the standard deviation is at a minimum as shown in Fig. 3.35.

Regression analysis would result in $n = 0.754$ with a value of $C = 0.0001185$ and the formula for $h_{\text{wtr}} = \frac{V_{\text{wtr}}^n}{C}$. Table 3.1 shows h_{wtr} versus mass flow rate of water.

The quality of the refrigerant entering the condenser also was estimated because h_{ref} is a function of the quality in the condenser. We based the inlet quality on the subcooled exit condition and the cooling capacity of the water side:

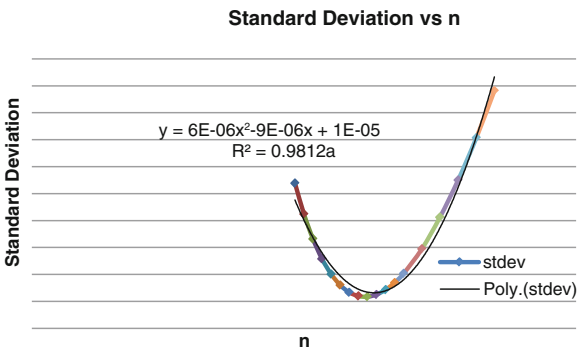

Fig. 3.35 Graph of standard deviation of C versus n

Table 3.1 Mass flow rate of water versus h_{wtr}

Volume flow rate (GPM)	Mass flow rate (kg/sec)	Velocity (m/s)	h_{wtr}
3	0.189	0.818	7249
4	0.252	1.090	9005
5	0.316	1.363	10656
6	0.379	1.635	12226
7	0.442	1.908	13733
8	0.505	2.180	15187
9	0.568	2.453	16598

$$X_{in} = (H_{in} - H_{out})/H_{fg} \tag{3.6}$$

where H's are the enthalpies of the respective streams. H_{out} is known, H_{fg} is calculated using the system pressure and qualities of $x = 1$ and 0, and H_{in} is calculated using the following formula:

$$H_{in} = Q_{water}/m_{ref} + H_{out} \tag{3.7}$$

Thermal Performance of a Tubular Micro-Groove Condenser

The flow manifold had the following dimensions: 2 mm width × 2 mm height with 3 mm flow length. The details are shown in Fig. 3.36, and a photograph of the manifold is shown in Fig. 3.37.

The condensation heat transfer coefficient as a function of saturation temperature is shown in Fig. 3.38. The refrigerant-side heat transfer coefficient increases with saturation temperature because of the increase in vapor density with saturation temperature. The condenser pressure drop was only about 0.07 bar for all of the tests (as shown in Fig. 3.39).

This condenser's high heat transfer coefficient would translate into a much lighter, more compact condenser for a given application. The volume for a tubular

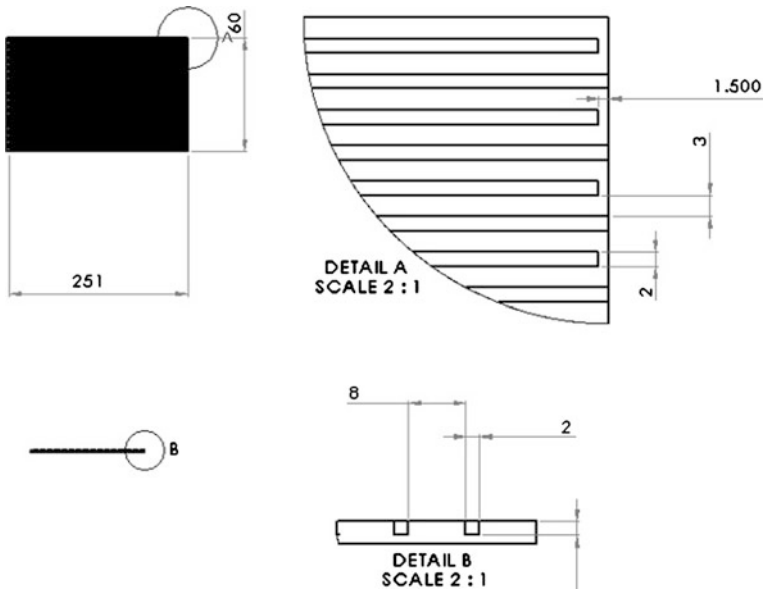

Fig. 3.36 Drawing manifold with 3 mm flow length

Fig. 3.37 Photograph of manifold with 3 mm flow length (edge view)

micro-groove condenser would be less than one-third (31 %) the volume of a state-of-the-art conventional condenser. The weight of the tubular condenser would be only about 38 % of a conventional condenser. Also, the pressure drop across the cooling fluid-side of the condenser would be about one-third that of a conventional fin-plate heat exchanger, which would in turn translate to reduce required operating power and energy losses.

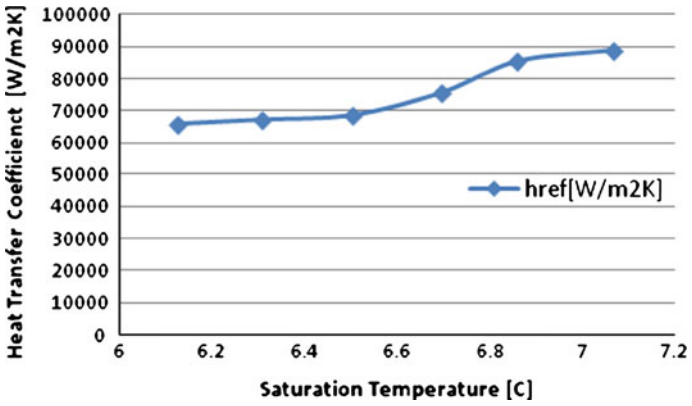

Fig. 3.38 Heat transfer coefficient as function of saturation temperature using new flow manifold with refrigerant R-134a

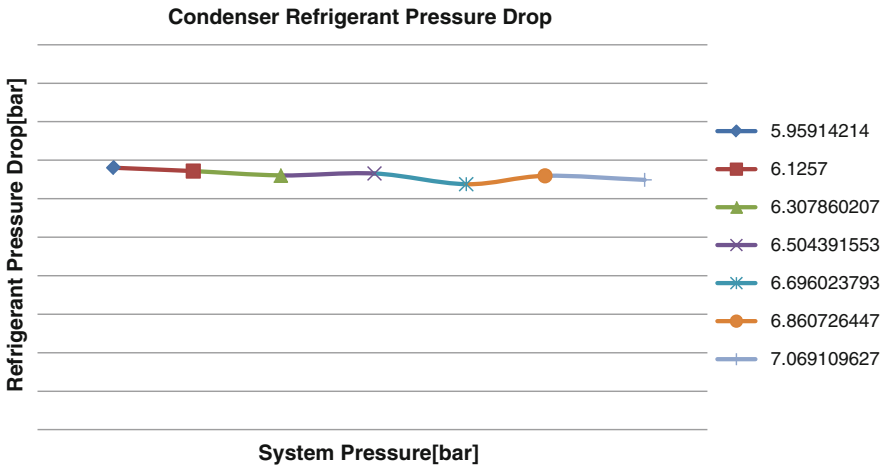

Fig. 3.39 Condenser refrigerant pressure drop as a function of system pressure with refrigerant R-134a

3.2 Microchannel Heat Pipes

Because advanced electronic equipment is decreasing in size, the circuit integration per unit area must increase, which in turn contributes to a rapid increase of heat generation rates. As a consequence, the operating temperatures of electronic components may exceed the desired temperature level, and if heat is not sufficiently removed, the failure rate of the equipment will cause an accelerated system failure. Due to the compactness of most modern electronic components, cooling devices also need to be small but highly effective in heat transport. Wicked heat pipes (or capillary-force-driven heat pipes) evaporate and condense the working

fluid and include complicated wick structures to circulate the working fluid. Although wicked heat pipes are prominent passive heat transfer devices, their performances decrease significantly as the thickness decreases below a certain limit—for instance, 2–3 mm. This is because there is a noticeable temperature drop across the flow direction when the vapor space volume is limited.

Recently, microchannel technology has been applied to the fabrication of micro heat pipes. Many experiments have been conducted on microchannel heat pipes. Cotter (1984) first introduced the concept of a micro heat pipe that did not include a complicated wick structure. Kang and Huang (2002) and Berre et al. (2003) have studied silicon micro heat pipes with a polygonal cross-section. The silicon micro heat pipes use the sharp edges of the polygonal groove for return of the condensate to the evaporator. Increases in effective thermal conductivities compared to silicon ranged from 10 to 80 %. Although silicon micro heat pipes are small and can overcome the thickness limitations of wicked heat pipes, they cannot handle a large amount of heat, and their performance has yet to be improved.

3.2.1 Micro-Pulsating Heat Pipes

Youn and Kim (2012) developed a micro-pulsating heat pipe that did not have a wick structure and instead contained rectangular microchannels forming a meandering closed loop. The heat was transferred from an evaporator to a condenser by means of the axial oscillation of liquid slugs and vapor slugs. This micro-pulsating heat pipe has progressed beyond research laboratories and is now under mass production. As shown in Fig. 3.40, micro-pulsating heat pipes with looped microchannels were fabricated by MEMS or micro-machining technology. The fabrication of the micro-pulsating heat pipe was completed by bonding the top cover plate and filling the pipe with a working fluid. Then the heat input and output were connected at the evaporation and the condensation sections, respectively. A total of 10 parallel, interconnected rectangular channels forming a meandering closed loop were engraved on the silicon wafer with a thickness of 1 mm. The top of the silicon wafer was covered by a transparent glass plate with a thickness of 0.5 mm to allow visualization of the internal thermohydrodynamic behavior in the micro-pulsating heat pipes. The silicon wafer and glass plate were bonded together using anodic bonding. A hole of 1 mm diameter was drilled on the top of the glass plate to evacuate the micro-pulsating heat pipes and fill the micro-pulsating heat pipes with working fluid. Figure 3.40 represents the fabricated micro-pulsating heat pipes and dimensions of the heat pipe. The overall micro-pulsating heat pipes had a length of 50 mm, width of 15.5 mm, and thickness of 1.5 mm. The width and height of the engraved rectangular channel were 1 and 0.6 mm, respectively, and the hydraulic diameter was 0.75 mm. Ethanol was used as a working fluid. The micro-pulsating heat pipes achieved maximum effective thermal conductivity of 600 W/m K and a maximum heat transport capability of 4 W.

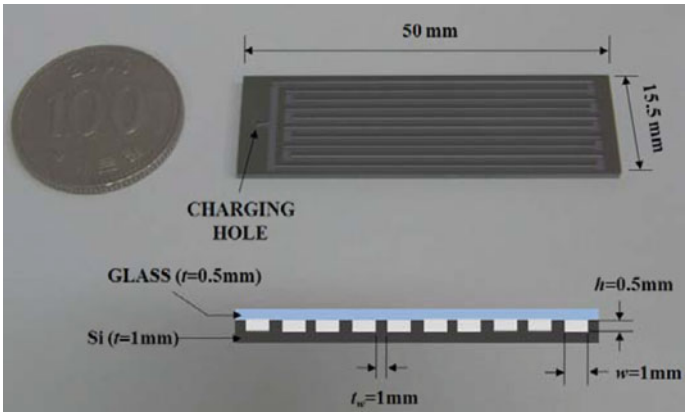

Fig. 3.40 Micro-pulsating heat pipe (Youn and Kim 2012)

As shown in Fig. 3.41a, the heat was transferred from the evaporator to the condenser sections by means of the axial oscillation of liquid slugs and vapor slugs. The micro-pulsating heat pipe is different from conventional heat pipes in design and working principle. There is no wick structure to return the condensed working fluid back to the evaporator section. The micro-pulsating heat pipe is made from a long meandering continuous capillary tube bent into many turns. The diameter of the tube is made sufficiently small that vapor plugs can be formed by capillary action as shown in Fig. 3.41b. The tube diameter that causes vapor plug and liquid slug arrangement (slug-train unit) is about 0.1–5 mm, and the critical diameter can be obtained (Akachi 1990) by

$$D_{\text{crit}} \leq 1.84\sqrt{\frac{\sigma}{g(\rho_l - \rho_v)}} \tag{3.8}$$

where σ is the surface tension, ρ_l is the liquid density, ρ_v is the vapor density, and g is the gravitational acceleration. If the tube diameter is too large, the liquid and vapor will tend to stratify. The micro-pulsating heat pipe operates in the following manner: the heat input increases the pressure of the vapor plug in the evaporator section; this pressure increase, in turn, pushes the neighboring liquid slugs toward the condenser section at low pressure. The heat is transported from the evaporator to the condenser by means of local axial oscillations and phase changes in the working fluids. A manufactured micro-pulsating heat pipe is shown in Fig. 3.42, in which the boundary between the liquid slugs and the vapor slugs is distinguishable.

The micro-pulsating heat pipe has many advantages, including high thermal performance and a maximum effective thermal conductivity of about 600 W/m·K, which is 3.5 times higher than that of silicon ($k = 162$ W/m·K) and 1.5 times that of copper ($k = 400$ W/m·K). It is possible to make a small, thin, and flat structure, and if a flexible material is used for the base and cover materials, it is possible to make a flexible micro-pulsating heat pipe because there is no wick structure.

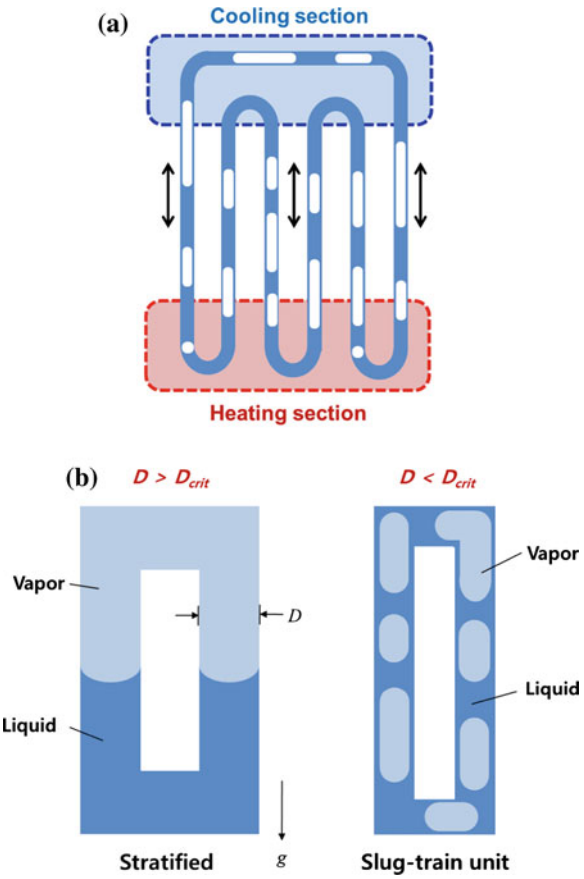

Fig. 3.41 **a** Working principle of micro-pulsating heat pipe. **b** Vapor and liquid arrangement according to tube diameter (Youn and Kim 2012)

3.2.2 Microchannel Flat Heat Pipes

The potential devices for which the flat micro heat pipes fabricated may be applied are mobile electronics such as small notebook PCs, PDAs, or cellular phones. Although conventional heat pipes use either wire mesh or sintered metal for the wick structure that is attached to the inner surface of a sealed metal housing, it is difficult to adopt the same approach in micro flat heat pipes, as MHP size cannot be reduced below a certain limit, for instance of 2–3 mm in thickness, due to the volume of the wick structure itself. Thus, the flat micro flat heat pipes should occupy as little space as possible to fit in the already small mobile device. Also, since the main heat source in an electronic device is a chip, and the sides of most chips are flat, the flat micro flat heat pipes are designed in a flat rectangular shape with a thickness of 1.5 mm.

Recently, Lim et al. (2008) developed a micro heat pipe with a microchannel groove wick structure using laser micro-machining technology. The structure of

Fig. 3.42 Top view of the micro-pulsating heat pipe with filling ratio of 50 % (Youn and Kim 2012)

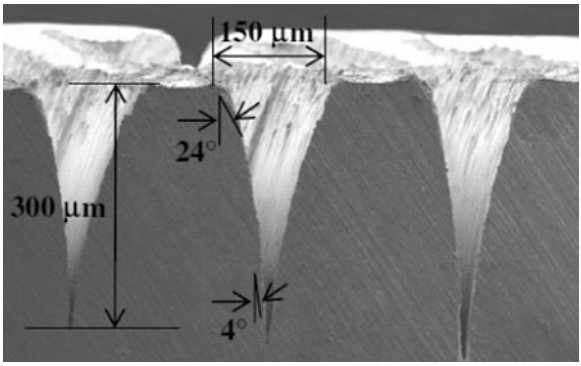

Fig. 3.43 Structure of microchannel grooves (Lim et al. 2008)

the microchannel grooves of a micro flat heat pipe is shown in Fig. 3.43. The microchannel grooves can be fabricated by laser micro-machining, MEMS, or LIGA technologies. The microgrooves of the micro flat heat pipe were fabricated on copper foil using a femtosecond laser micromachining technique. A commercial chirped pulse amplification laser system and a translation XYZ stage were used to fabricate the grooves under normal atmospheric air. The laser beam was focused on the workpiece using a 10x objective lens, and the workpiece was firmly attached on the translation stage using tape. The microgrooves, which serve to facilitate liquid passage during operation, were machined on the top and bottom plates. The width, depth, and length of each microgroove were about 150, 300, and 50 mm, respectively, and 16 grooves were produced on each plate.

As shown in Fig. 3.44, the fabrication of the micro flat heat pipe was completed by bonding the top cover plate and filling the pipe with a working fluid. Then the heat input and output were connected to the evaporation and the condensation sections, respectively. A manufactured micro-pulsating heat pipe is shown in Fig. 3.45. The working principle of the micro flat heat pipe is the same as that of a conventional heat pipe with a porous wick structure. The heat is transferred from an evaporator to a condenser. When one end of the heat pipe is heated, the working fluid inside the pipe at that end evaporates and increases the vapor pressure inside

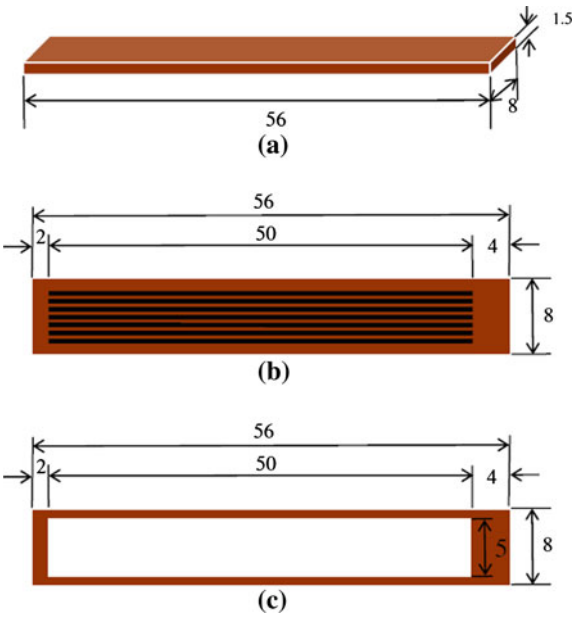

Fig. 3.44 Structure of **a** the overall micro flat heat pipe; **b** the top and bottom plates with microgrooves; and **c** the middle plate for vapor passage (unit: mm)

the cavity of the heat pipe. The latent heat of evaporation absorbed by the vaporization of the working fluid reduces the temperature at the hot end of the heat pipe. The heated vapor moves to the condensation section and condenses back into a liquid at the cold interface, releasing the latent heat. The liquid then returns to the hot interface through the capillary action of the microchannel grooves, where it evaporates once more and repeats the cycle. The micro flat heat pipe has many advantages, including its small, thin, and flat structure. It also has high thermal performance, with a maximum heat transfer rate of 8 W under stable operation and 13 W at the dryout point, as shown in Fig. 3.46.

Recently, Ohadi et al. (2011) designed a microchannel surface-based heat exchangers for a sodium heat-pipe solar energy receiver for a solar-powered Stirling engine generator. Usually, the heat-pipe surface is made of very thin inconel and is sintered very carefully to avoid defects. Any defects due to improper sintering dry out that area of the heat pipe surface immediately due to concentrated solar energy on the heat pipe receiver. In their current design, the micro-grooved receiver surface was constructed of a solid nickel plate (as shown in Fig. 3.47), and thus the micro-grooves cannot be separated from the heated surface. The nickel plate also ensures faster, effective heat transfer without any dryout through the sodium heat pipe from the receiver to the Stirling engine heater head.

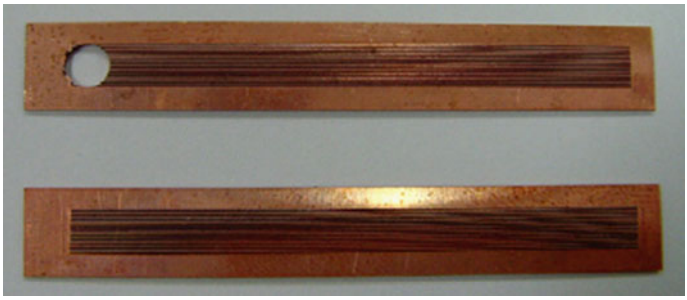

Fig. 3.45 Top view of the micro flat heat pipe (Lim et al. 2008)

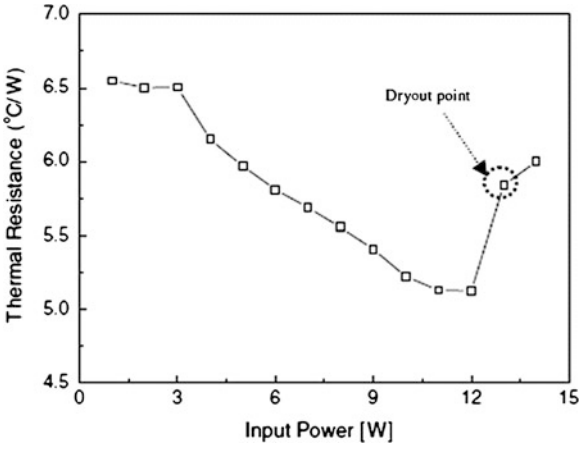

Fig. 3.46 Thermal resistance change at the dryout point of the micro flat heat pipe (Lim et al. 2008)

3.2.3 Counter-Stream-Mode Oscillating Flow Micro Heat Pipe

Nishio et al. (1995) proposed counter-stream-mode oscillating flow (COSMOS) heat pipes, wherein a meandering channel is employed to make an out-of-phase oscillating flow in neighboring channels. The COSMOS heat pipes can provide an enhanced heat diffusion effect compared with conventional heat pipes. Sugimoto et al. (2005) fabricated a micro-COSMOS heat spreader and verified that the theoretical model for the thermal performance of the COSMOS heat pipe proposed by Nishio et al. (1995) accurately predicted the thermal performance of the fabricated micro-COSMOS heat spreader. The heat spreader, fabricated by silicon micromachining, had 14 folded meandering Si grooves with total length of 700 mm, width of 575 μm, depth of 400 μm, and wall thickness between the adjacent channels of 150 μm. The heat spreader was connected to two

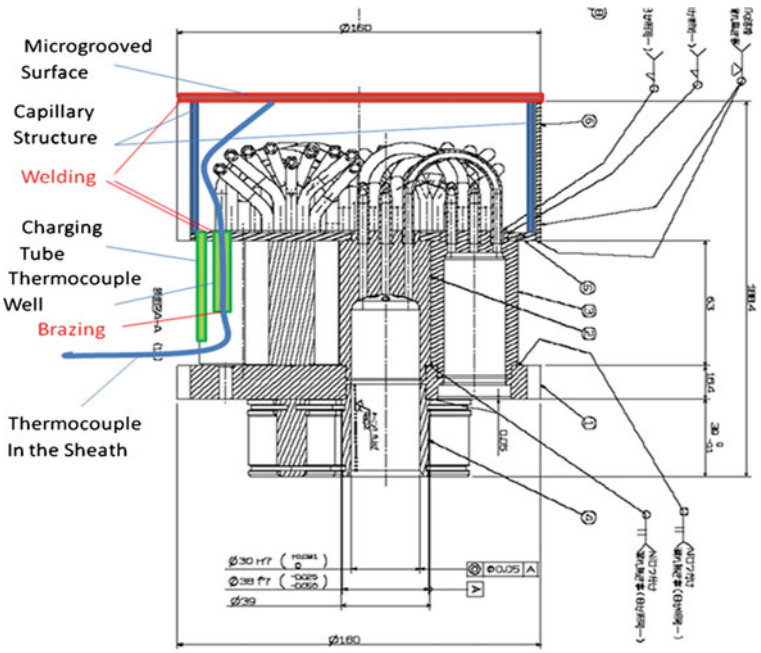

Fig. 3.47 Schematic of solar Stirling engine generator with micro-grooved sodium heat pipe receiver

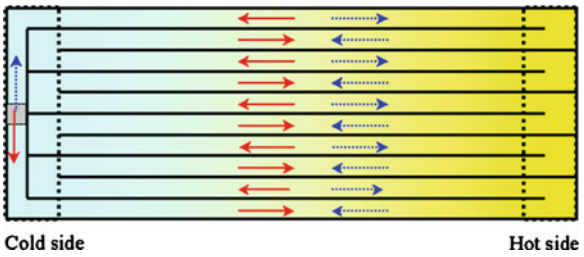

Fig. 3.48 Working principle and geometry of COSMOS heat pipe (Nishio et al. 1995)

piezoelectric pumps. The total device size was 86 × 57 mm^2, and the effective cross-section of the heat pipe was 0.5 × 10 mm^2.

The operational principle and structure of the COSMOS heat pipe type heat spreader are shown in Fig. 3.48. Heat is transferred by thermal conduction between adjacent microchannels and does not rely on phase change. The fluid is driven by oscillation through densely arranged meandering microchannels placed between a heat source and a heat sink. The COSMOS operational principle is completely different from the loop heat pipe. Theoretically, the COSMOS heat pipe has higher effective thermal conductivity than the conventional heat pipes and

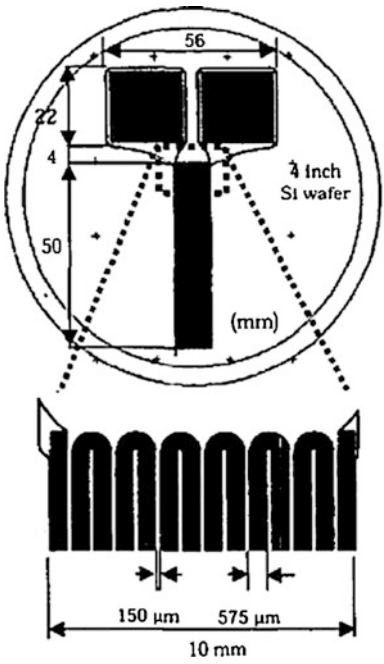

Fig. 3.49 Piezoelectric pump of the COSMOS heat pipe (Nishio et al. 1995)

thus may be suitable for miniaturization of thermal equipment. Furthermore, the cooling efficiency can be controlled continuously by controlling the oscillation frequency or driving fluid volume. This is a unique feature of this device that makes it possible to control the temperature of a heat source by varying the heat spreading performance, transporting heat from the heat source to the heat sink.

The COSMOS heat pipe requires an additional external power source to sustain the liquid oscillating motion. To realize a pump with the performance mentioned above and a size thin enough to be eventually imbedded in a small space of an electronic device, a dual piezoelectric pump configuration was adopted by Nishio et al. (1995). Two pumps were connected to both ends of the channel, as schematically shown in Fig. 3.49, and operated simultaneously to drive the fluid by push–pull operation. The piezoelectric pump was constructed by bonding the PZT plate with thickness of 120 μm and size of 20 mm on the Si diaphragm with thickness of 100 μm and size of 22 mm. These thicknesses and sizes were based on the FEM analysis. The COSMOS heat pipe demonstrated a temperature gradient of 500 K/m and a heat transport rate of 20 W with water as the working fluid. As shown in Fig. 3.50, the effective thermal conductivity was calculated as 9×10^3 W/mK, which is 23 times higher than that of copper.

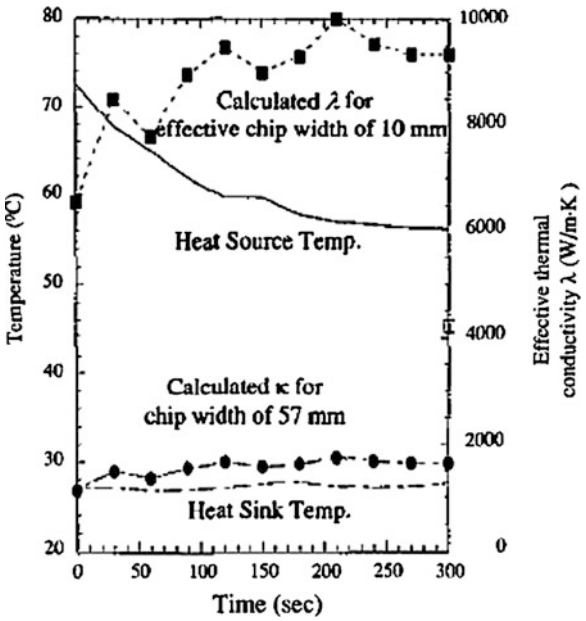

Fig. 3.50 Measured performance of the COSMOS heat pipe (Nishio et al. 1995)

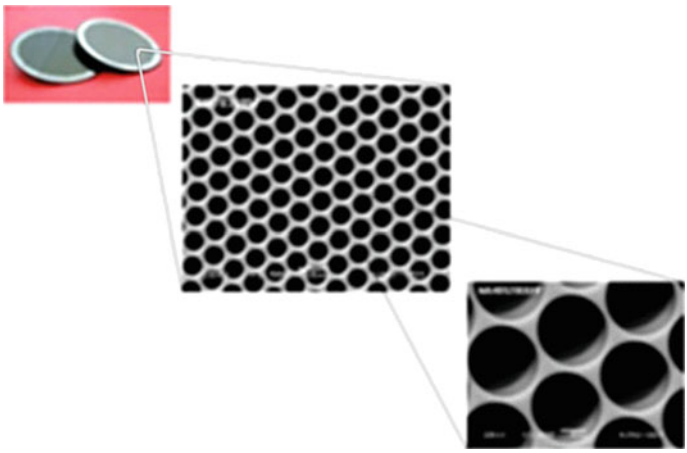

Fig. 3.51 Microchannel plate (Tectra Inc.)

3.3 Microchannel Heat Plates

A microchannel plate (MCP) is a planar component used to detect particles (electrons or ions) and impinging radiation (ultraviolet radiation and X-rays), as shown in Figs. 3.51 and 3.52. A typical MCP consists of about 10,000,000 closely packed channels of common diameter, formed by drawing, etching, or firing in

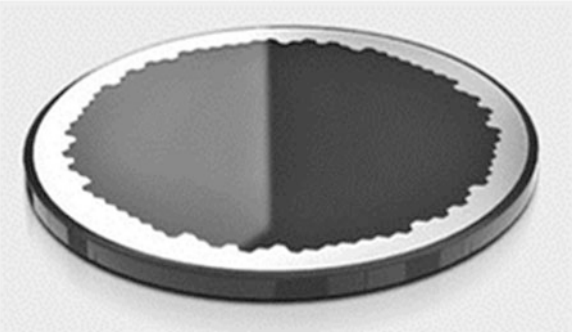

Fig. 3.52 Microchannel plate for night vision (Directindustry Inc.)

hydrogen, forming a lead glass matrix. Typically, the diameter of each channel is ~10 microns. Each channel acts as an independent, continuous dynode photomultiplier. MCPs are widely used to intensify low-light signal inside various image detectors. Industries for MCP applications range from astronomy to aerospace, machine-building, experimental physics, chemistry, biology, medicine, and ecology.